Holographic patterning of high-performance on-chip 3D lithium-ion microbatteries

Hailong Ning[a], James H. Pikul[b], Runyu Zhang[a], Xuejiao Li[a], Sheng Xu[a], Junjie Wang[a], John A. Rogers[a,b], William P. King[a,b], and Paul V. Braun[a,b,1]

[a]Department of Materials Science and Engineering, University of Illinois at Urbana–Champaign, Urbana, IL 61801; and [b]Department of Mechanical Science and Engineering, University of Illinois at Urbana–Champaign, Urbana, IL 61801

As sensors, wireless communication devices, personal health monitoring systems, and autonomous microelectromechanical systems (MEMS) become distributed and smaller, there is an increasing demand for miniaturized integrated power sources. Although thin-film batteries are well-suited for on-chip integration, their energy and power per unit area are limited. Three-dimensional electrode designs have potential to offer much greater power and energy per unit area; however, efforts to date to realize 3D microbatteries have led to prototypes with solid electrodes (and therefore low power) or mesostructured electrodes not compatible with manufacturing or on-chip integration. Here, we demonstrate an on-chip compatible method to fabricate high energy density (6.5 µWh cm^{-2}·µm^{-1}) 3D mesostructured Li-ion microbatteries based on LiMnO$_2$ cathodes, and NiSn anodes that possess supercapacitor-like power (3,600 µW cm^{-2}·µm^{-1} peak). The mesostructured electrodes are fabricated by combining 3D holographic lithography with conventional photolithography, enabling deterministic control of both the internal electrode mesostructure and the spatial distribution of the electrodes on the substrate. The resultant full cells exhibit impressive performances, for example a conventional light-emitting diode (LED) is driven with a 500-µA peak current (600-C discharge) from a 10-µm-thick microbattery with an area of 4 mm^2 for 200 cycles with only 12% capacity fade. A combined experimental and modeling study where the structural parameters of the battery are modulated illustrates the unique design flexibility enabled by 3D holographic lithography and provides guidance for optimization for a given application.

energy storage | microelectronics | miniature batteries | lithium-ion batteries | interference lithography

Microscale devices typically use power supplied off-chip because of difficulties in miniaturizing energy storage technologies (1, 2). However, a miniaturized on-chip battery would be highly desirable for applications including autonomous microelectromechanical systems (MEMS)-based actuators, microscale wireless sensors, distributed monitors, and portable and implantable medical devices (3–8). For many of the applications, high energy density, high power density (charge and/or discharge), or some combination of high energy and power densities is required, all characteristics which can be difficult to achieve in a microbattery due to size and footprint restrictions, and process compatibilities with the other steps required for device fabrication. Although 2D thin-film microbatteries (typical thickness of a few micrometers) can deliver high power, they require large (often cm^2) footprints to provide reasonable energies (9). Making the electrodes thicker boosts the theoretical areal energy density but the resultant increases in electron and ion diffusion lengths reduce the effective power and energy densities. Efforts to improve microbattery performance have focused on increasing the electrode surface area and active material loading in the third dimension. Electrodes based on high-aspect-ratio micropillar structures, realized via methods including electrodeposition, polymer pyrolysis, and vapor deposition techniques, have been demonstrated (10–14). Despite the improved energy density compared with 2D batteries, because

the micropillar electrodes are solid, the power and effective energy density is still limited due to the resultant long ion and electron diffusion pathways. Mesostructured 3D electrodes derived from nanowires or nanotubes have potential for achieving high energy and power densities, but difficulties in synthesis and full-cell assembly have limited these electrodes to half-cell demonstrations (15–18).

As we demonstrated via a colloidal templating strategy (19–21), electrodes consisting of a layer of electrolytically active materials directly grown on a mesostructured 3D porous current collector can offer both high energy and power densities by providing efficient electron pathways, short solid-state ion diffusion lengths, and a pore network for Li-ion transport. Unlike for a micropillar, all of the major internal resistances of the microbattery can be simultaneously minimized. The colloidally templated 3D mesostructured electrodes were first fabricated in a half-cell configuration, and the resulting electrode indeed delivered supercapacitor-like power (e.g., 40% energy discharge in 3 s) while maintaining battery-like energy (19). We subsequently fabricated a microbattery (full cell) with an unprecedented 2,000× increase in power compared with previous microbatteries (22) via a similar approach. However, colloidally templated microbatteries contain a number of serious limitations. From a purely practical standpoint, a fabrication approach that involves growth of a colloidal crystal from a colloidal suspension on a substrate is unlikely to be acceptable in a manufacturing environment, because it is slow, and submicrometer colloidal particles are generally unwelcome in a microfabrication facility. The mesostructure and connectivity of the colloidally templated system is severely restricted by the close-packed particles, allowing almost no freedom to alter the structure of a unit cell. Finally, all colloidal crystals contain defects (e.g., cracks), which end up in the final

---

Significance

Microscale batteries can deliver energy at the actual point of energy usage, providing capabilities for miniaturizing electronic devices and enhancing their performance. Here, we demonstrate a high-performance microbattery suitable for large-scale on-chip integration with both microelectromechanical and complementary metal-oxide–semiconductor (CMOS) devices. Enabled by a 3D holographic patterning technique, the battery possesses well-defined, periodically mesostructured porous electrodes. Such battery architectures offer both high energy and high power, and the 3D holographic patterning technique offers exceptional control of the electrode's structural parameters, enabling customized energy and power for specific applications.

Fig. 1. Schematic illustrations and images of 3D microbatteries enabled by combining 3D holographic and conventional photolithographies. (*A*) Three-dimensional microbattery fabrication process (*I*): create 3D lattice (SU-8) on an ITO substrate using holographic lithography (*II*), infiltrate the 3D holographic structure with another photoresist (AZ9260) (*III*), photopattern the second photoresist to define the microbattery electrode (*IV*), invert the photoresist template by nickel electrodeposition (*V*), remove the photoresist template by oxygen RIE and etch the exposed ITO layer by methane RIE, and (*VI*) sequentially electroplate nickel–tin (Ni–Sn) and manganese oxide on the interdigitated 3D nickel current collector as anode and cathode, followed by a selective lithiation with a drop of LiNO₃/LiOH molten salt to produce LMO. (*B*) Scanning electron microscopy (SEM) cross-section of the photopatterned AZ9260 resist embedded inside the 3D holographic lattice. (*C*) SEM cross-section of a single digit of the interdigitated nickel scaffold. (*Insets*) Top-down optical micrograph (*Right*) and an enlarged view (*Left*) of the interdigitated nickel current collector (area: 4 mm²). (*D*) Cross-section SEM image of the interdigitated electrodes that alternate between LMO cathode (*Left Inset*) and Ni-Sn anode (*Right Inset*).

electrode structure as solid elements (the inverse of a crack). These solid elements locally limit ion transport and make capacity matching between anode and cathode difficult, which may in part be why the cycle life of the colloidally templated microbattery was low. In contrast with colloidal assembly and other 3D fabrication techniques such as direct laser (ink) writing (which produces 3D structures in a point-to-point or layer-by-layer fashion) (23, 24), 3D holographic lithography generates periodic, defect-free features (50~1,000 nm) in a one-step exposure (~ seconds) over an area that is linearly proportional to the beam size. It can create a variety of complex 3D structures by varying the beam patterns and exposure conditions. Although accurate control on the interfering optical beams is required to construct 3D holographic lithography, recent advances have significantly simplified the required optics, enabling creation of structures via a single incident beam and standard photoresist processing, making it highly scalable and compatible with microfabrication (25, 26).

Here, we describe a flexible and deterministic 3D fabrication route which combines 3D holographic lithography with conventional photolithography to create microbatteries with good cycle lives, and high power and energy densities using complementary metal-oxide–semiconductor (CMOS) and microfluidic device-compatible processing steps. The holographic lithography creates a defined periodically mesostructured 3D lattice, whereas the conventional photolithography defines a set of 2D solid structures that divide the 3D lattice into an interdigitated pattern. The combination of these two lithography processes provides comprehensive control of the electrode mesostructure and spatial arrangement, enabling formation of flat-sided and topped 3D current collectors with independently deposited high-quality cathode and anode active materials. The resultant full cells exhibit energy and power densities up to 6.5 µWh cm⁻²·µm⁻¹ (energy-optimized electrode spacing) and 3,600 µW cm⁻²·µm⁻¹ (power-optimized electrode spacing), with less than 5% cell-to-cell distribution. The cells retain at least 80% of the initial capacity after cycling 100 times at various rates, and 88% of the initial capacity after driving a light-emitting diode (LED) for 200 cycles. The capacity for fast charging and discharging endues the microbattery with rather unexpected capabilities for a battery which is only 2 mm on a side and ~10 µm thick, for example the battery could repeatedly (>200 cycles) drive a conventional LED with a 600-C

peak current (~0.5 mA). A combined experimental and modeling study where the structural parameters of the battery are modulated illustrates the unique design flexibility enabled by 3D holographic lithography and provides guidance for optimization for a given application.

Design and Fabrication of Deterministically Structured 3D Microbatteries

The fabrication of the microbattery combines both 3D holographic lithography and 2D photolithography. In principle, both these lithographic steps can be performed on a single negative photoresist film. However, a holographically defined 3D lattice made of negative photoresist (e.g., SU-8) suffers from a volume shrinkage of ~40% during development, whereas the 2D pattern formed from the same photoresist only shrinks ~7% during development, resulting in a large structural distortion. To circumvent this, a thick 3D lattice is formed using SU-8, and the SU-8 network is subsequently infiltrated with another photoresist to pattern the electrodes as illustrated in Fig. 1*A*. Specifically, a 3D holographically defined lattice (typical periodicity: ~1 µm; porosity: ~40%) is created on indium tin oxide (ITO)-coated glass by four interfering laser beams arranged in an umbrella geometry (27, 28). Because the intensity, polarization, and angle of each beam can be individually defined, this method offers considerable flexibility in the design of the holographic structure. The electrode distribution is then photolithographically defined with a positive photoresist (AZ9260). Fig. 1*B* shows the cross-sectional view of the resultant structure, where the second resist forms solid straight walls inside the 3D lattice. Next, Ni is electrodeposited partially through the porous SU-8 lattice. Notably, compared with our previous microbattery design where the Ni electrodeposition step created hemispherical-shaped electrode digits due to the unconfined concurrent vertical and lateral growth of the Ni scaffold (22), which was undesirable due to inefficient use of the device space and potential for short formation due to dendrite growth during Ni electrodeposition, the Ni growth here is confined by the vertical photoresist walls, providing independent control over the scaffold height (Ni plating time) and width (photolithographic step). The microbattery current collector is revealed after the photoresist template is removed by oxygen reactive ion etching (RIE). The final current collector consists of a 4-mm² area interdigitated 3D porous Ni
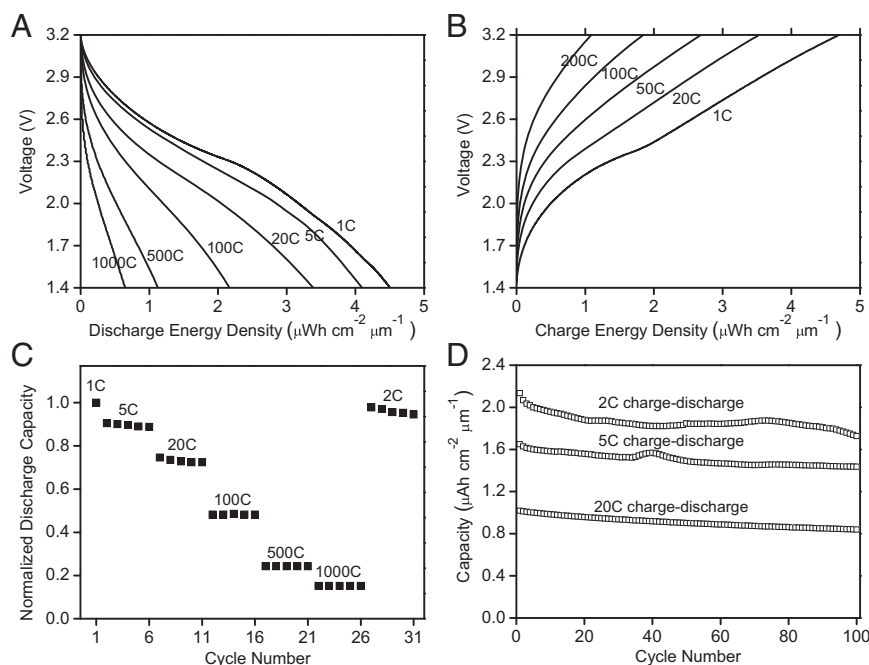
Fig. 2. Performance of 3D microbatteries under various charge–discharge rates. (*A*) Discharge voltage profiles of a microbattery at rates ranging from 1 to 1,000 C. (*B*) Charge voltage profiles of a microbattery at 1 to 200 C. (*C*) Capacity of a microbattery for the first 31 cycles at 1-C charge and the noted discharge rates (normalized to the 1-C discharge). (*D*) Capacity of microbatteries that are cycled at various C rates 100 times.

scaffold (Fig. 1*C*). Each individual electrode digit has a rectangular cross-section, which is ~10 μm high and ~60% porous. Unless otherwise mentioned, the electrode digits are 35 μm wide and the gap between electrodes is 15 μm. After removal of the photo-resist template, the exposed ITO layer on the substrate between the electrode digits is etched using methane RIE, electrically isolating the anode and cathode current collectors. The active materials, Ni–Sn (90% tin, ~70 nm thick), and MnO_2 (~100 nm thick) are sequentially electroplated onto the Ni scaffold as anode and cathode, respectively (Fig. 1*D*). The MnO_2 cathode is then selectively lithiated in LiOH and $LiNO_3$ molten salt, followed by rinsing with water and drying.

Our group has recently investigated the half-cell cyclabilities of lithiated MnO_2 (LMO) and Ni–Sn on macroscopic colloidally templated 3D Ni scaffolds (19, 29). Our LMO cathodes generally exhibit good cycle lives with capacity fades of 10% or less over 50 cycles. The Ni–Sn anode often fades below 90% within the first few cycles but then fades at a much slower pace in subsequent cycles. The large capacity loss in the first few cycles is probably caused by solid electrolyte interphase (SEI) formation (30). Due to the large surface area of our microbatteries, the initial SEI formation can degrade a significant amount of electrolyte, leading to an excessive lithium loss. To produce a stable SEI layer without consuming the limited lithium source, the Ni–Sn anode is independently cycled versus lithium metal six times in a large electrolyte reservoir before packaging. Following this, a drop of fresh electrolyte is cast onto the microbattery, and the microbattery is capped with polydimethylsiloxane (PDMS) and a glass slide, and sealed using a UV resin. The battery is then stable in air for at least a few days. Reports on packaging of liquid electrolyte-based microbatteries have previously demonstrated scalability and long-term stability (31, 32), making us optimistic that our design could also be packaged to provide extended stability.

Electrochemical Testing

The packaged microbattery is galvanostatically tested between 3.2 and 1.4 V. Fig. 2*A* shows the discharge voltage profiles of a microbattery that is charged at 1 C and discharged at various C rates (1 C stands for charging–discharging the battery in an hour; at a C rate of N, the cell is charged–discharged at N times the 1 C current). The cell possesses a volumetric energy density of 4.5 μWh cm^{-2}·μm^{-1} at 1 C and a significant retention of its 1-C energy at high power. At 1,000 C, it provides a 0.6 μWh cm^{-2}·μm^{-1} energy and a 3,600 μW cm^{-2}·μm^{-1} power. The interdigitated 3D porous electrodes also enable fast charging. As shown in Fig. 2*B*, when the cell is charged at different rates and discharged at 1 C, it reaches ~80% state of charge (SOC) at a 20-C charge and ~50% SOC at a 50-C charge.

Practical microbattery applications probably require a cycle life of at least a few hundred charge–discharge cycles. Whereas tin, its alloys, and its oxides have attracted considerable attention for their high energy density, it is also well-known that these anode materials experience a large (~260% for tin) volume change upon alloying–dealloying that can continuously crack the SEI passivated surface leading to electrolyte decomposition, or can lead to active material delamination, both of which result in a severe capacity fade during cycling (33–35). In our microbatteries, the capacities of cathode and anode are carefully matched so that LMO cycles between 3.5 and 2.2 V versus Li/Li$^+$ and Ni–Sn cycles between 0.3 and 0.8 V versus Li/Li$^+$ (Fig. S1). We find that careful control of the Ni–Sn cycling range, in conjunction with the 3D Ni scaffold, significantly improves the cyclability, probably because the scaffold significantly relieves the cycling-induced stress in the film. Under these cycling conditions, the full cell exhibits at least 80% capacity retention over 100 cycles at a variety of charge and discharge rates, which is considerably better than previously demonstrated 3D full-cell microbatteries, which typically either cycled only a few times or faded quickly after tens of cycles (14, 22, 32, 36). Fig. 2*C* presents the normalized discharge capacity of a microbattery that is charged at 1 C and discharged at high rates. The battery only shows a small capacity loss after 25 fast discharge cycles (from 5 to 1,000 C). Microbatteries are also cycled at 2 C, 5 C, and 20 C, respectively (Fig. 2*D*), and at least 80% of the initial capacity is retained after 100 cycles in all three cases and 77% is retained

after 200 cycles at 20 C (cells are not tested to 200 cycles at other C rates).

To demonstrate the capability of our microbatteries in a simple device application, a packaged cell is connected to a single-pole–double-throw (SPDT) relay that charges the microbattery potentiostatically at 3.2 V for 5 min (by two AA batteries) and sequentially discharges it to a red LED for 10 s. As shown in Fig. 3A (and Movie S1), even though the microbattery has a volume of only 0.04 mm^3 (excluding packaging) and a capacity of only 0.83 µAh, it provides sufficient power and energy to repeatedly drive the LED at least 200 times. The cell provides a peak current of ~480 µA (~600 C) and the depth of discharge is ~21.6% in each cycle (Fig. 3B). As noted in Fig. 3C, the peak and integrated output current barely change throughout the cycling, indicating minimal capacity fade, a necessary attribute for many applications.

Holographic Optimization of Energy and Power

An important asset in combining 3D holography with 2D photolithography for microbattery fabrication is the ease by which the electrode morphology and characteristic dimensions can be controlled, enabling investigation of the physics that regulates the microbattery energy and power. At some point, the power of an interdigitated battery decreases as the electrode digits become wider due to an increased ion diffusion distance inside the electrodes. However, for a battery that has a fixed footprint and electrode spacing (below some minimum spacing, electrical shorts may occur), wider electrode digits provide a greater total energy as the number of gaps between electrodes is reduced and more space is filled with active materials (Fig. 4A). Here, we investigate the trade-off between energy and power by fabricating cells with various digit widths (W) but the same total area and electrode spacing (S = 15 µm). By tightly capping the prismatic-shaped electrodes with PDMS stamps (Fig. S2), ions are forced to travel only in the lateral direction during cycling, enabling drawing direct correlations between electrode digit width, energy, and power. Fig. 4B shows the high-rate discharge capacity of cells containing 35-µm-, 60-µm-, and 110-µm-wide electrode digits. At a low rate of 1 C the microbattery capacity increases as the digit width increases, going from ~2.1 µAh·cm^{-2}·µm^{-1} (energy density 4.5 µWh cm^{-2}·µm^{-1}) for a 35-µm electrode width to ~2.9 µAh cm^{-2}·µm^{-1} (energy density 6.5 µWh cm^{-2}·µm^{-1}) for a 110-µm electrode width (about what would be calculated assuming complete discharge of active material). As the C rate increases, the capacity of the microbattery with the widest electrodes falls off most significantly. For example, at 20 C the cell with 60-µm width delivers the most charge among the three, and by looking at the capacity retentions (normalized to 1-C discharge) it is the largest electrode width that has lost the most capacity (capacity retentions of 61%, 53%, and 32% for the 35-µm-, 60-µm-, and 110-µm-wide electrodes, respectively). The large decrease at the 110-µm width suggests that liquid-phase ion diffusion is becoming insufficient for this microbattery at this discharge rate. At higher C rates, the capacity of the microbatteries with wider electrodes continues to fall off faster than the narrow electrode microbattery.

To assist in interpretation of the influence of electrode parameters on battery performance, the microbattery is simulated using a simple 1D COMSOL model (see SI Text and Table S1 for details) in which the cell capacity is calculated for electrode digit widths ranging from 5 to 170 µm (Fig. 4B). Whereas the simulation only captures the trends in cell behavior, it does provide important information. At 1 C and below, the cell capacity scales with the digit width following W/(W+S) as a result of a quasi-equilibrium discharge (observed in both simulation and experiment). In both theory and experiment, there exists a critical width (Wc) for each higher rate. Below Wc, capacity still closely obeys W/(W+S). At Wc, the capacity reaches a maximum. Above Wc, the electrolyte severely polarizes near the center of the electrodes during discharge (Fig. S3), leading to a marked
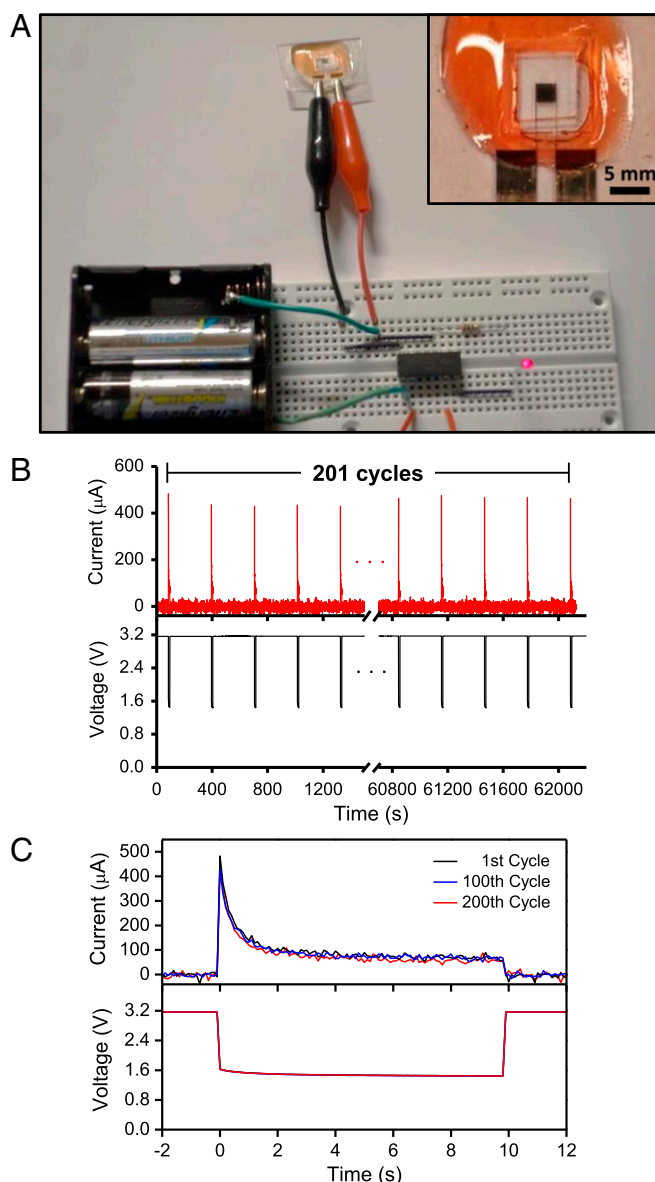

Fig. 3. Demonstration where microbattery is controlled by an SPDT relay that periodically discharges it to a red LED for 10 s and charges it with two AA batteries for 5 min. (A) Optical image of the demonstration setup. Picture taken at the moment the microbattery is connected to the LED (see Movie S1 for the full charge–discharge cycle). (Inset) Optical image of the microbattery. (B) Current and voltage profiles of the microbattery that is cycled by the relay 201 times. (C) Output current and voltage profiles for three representative discharges to the LED. The LED produces a visible light output for the full 10 s.

increase of the overpotential and prematurely ending the discharge. The simulation appears to capture Wc, although it does not capture the capacity well at intermediate C rates. It is clear that the decrease of power for cells with large digit width is attributed to the insufficient liquid-phase ion diffusion. The critical width at a given discharge rate, which maximizes the energy density without depleting ions inside electrodes, can be estimated by

$$\sqrt{D_0 \cdot (\varepsilon/\tau) \cdot (3{,}600/C-\text{rate})}, \qquad [1]$$

where D_0, ε, and τ are the electrolyte diffusion coefficient, electrode porosity, and tortuosity, respectively. Eq. 1 suggests that
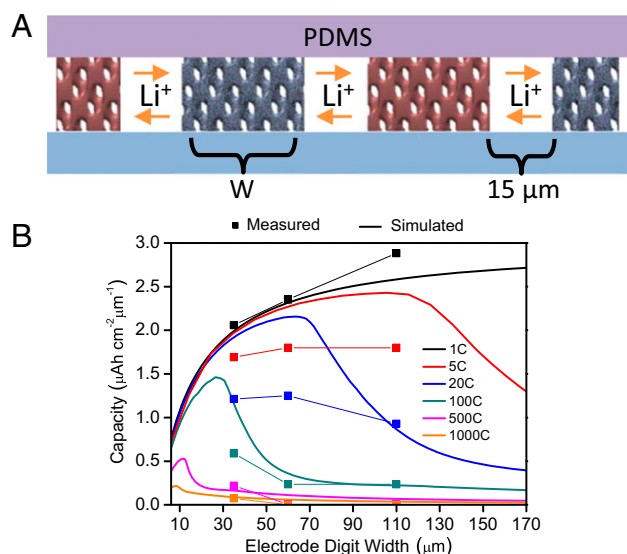
Fig. 4. Influence of electrode digit width on the performance of 3D microbatteries. (*A*) Schematic illustration of the ion transport inside the microbatteries. (*B*) Measured (scattered points) and simulated (lines) capacity as a function of electrode digit width at C rates ranging from 1 to 1,000.

optimization of the effective liquid-phase diffusion in the microbattery should focus on controlling the electrode porosity and tortuosity. In our holographically templated microbatteries, the electrode porosity can be easily tuned by the exposure dose during the fabrication of the holographic templates. Fig. 5*A* shows the simulated (see *SI Text* for details) structures of nickel current collectors with 30%, 40%, and 50% filling fractions, which are inverted from SU-8 templates with 70%, 60%, and 50% filling fractions, respectively. Three cells with these nickel filling fractions are fabricated and tightly capped with PDMS stamps (the filling fraction of SU-8 templates is determined by their characteristic peaks in reflection optical spectroscopy). The electrode tortuosity varies with porosity (Fig. S4) and is also strongly related to the geometric shape of the unit cell (37). The tortuosity of the electrodes tested in Fig. 5*B* ranged from 1.5 (most porous) to 3 (least porous). As expected, the cell with the lowest tortuosity (largest porosity) exhibits the best power performance (Fig. 5*B*). As our simulations show, ion depletion in the electrolyte only becomes important for the wider electrode at high C rates, and thus it is in these electrodes where tortuosity matters. For a given lattice parameter, the surface area is also a weak (varies about 10% over the range of samples presented in Fig. 5*B*) function of porosity (Fig. S4).

Discussion

A holographically defined interdigitated 3D microbattery has a number of unique attributes for on-chip energy storage. It is both highly scalable and compatible with microelectronic processing because it uses many of the same materials and procedure common in conventional photolithography. Although here a four-beam holographic strategy is used, which is not a standard lithographic process, holographic exposures have also been demonstrated using both prism and phase-mask methods that can be performed using a standard photolithographic process (25, 26, 38). Compared with conventional battery electrode fabrication methods (e.g., slurry tape-casting), which are difficult to scale to the millimeter size and below, the template-assisted electrodeposition provides a viable path for creating miniaturized electrodes with high-quality active materials conformally attached to 3D mesoporous current collectors. An attribute of a holographic design is the ability to independently modulate the lattice symmetry and the lattice constant.

In our 3D microbattery design, the tortuosity is below 3, and thus whereas further reductions in tortuosity may not be meaningful, it is interesting to speculate if certain symmetries may better mitigate the mechanical stresses in anode materials which undergo large volume changes with cycling, such as tin and silicon (39). The lattice symmetry and the lattice constant dictate the internal surface area, which is an important parameter, as the volumetric energy density is proportional to the product of the active material thickness and the surface area of current collectors. Whereas the active material thickness may be limited to a few hundreds of nanometers to achieve fast solid-state diffusion, and thus a high power, the high surface area of the current collector results in a structure with a high energy density, even with a thin active material coating.

Because the areal energy density scales with the electrode height, approaches compatible with tall electrodes are important when the device footprint area is limited. Here, we have demonstrated the concept with an ~10-μm-thick electrode; however, this should not be an upper bound. Tens, and even hundreds, of micrometer-thick holographic structures have been fabricated using advanced photoresists that have low absorption and shrinkage but high sensitivity (40–42). Whereas 2D thin-film microbatteries can deliver a power density as high as 10^4 μW/cm^2 (9), they have to expand their footprint to increase the total stored energy and power, because making the electrodes thicker reduces the power. The 10-μm-thick holographically defined microbattery presented here delivers a power of 3.6×10^4 μW/cm^2, and, unlike a thin-film microbattery, both energy and power scale proportionally with thickness.

Conclusions

We have developed a method to fabricate 3D microbatteries that is highly scalable and compatible with CMOS and MEMS processes. The fabrication uses both 3D holographic lithography and conventional photolithography to create the microbattery template, followed by template-assisted electrodepositions to produce thin layers of active materials that are conformally grown on 3D current collectors. The resultant microbattery, which consists of interdigitated microscaled electrodes with mesostructured pores and desired electrode shape, exhibits superior energy and power
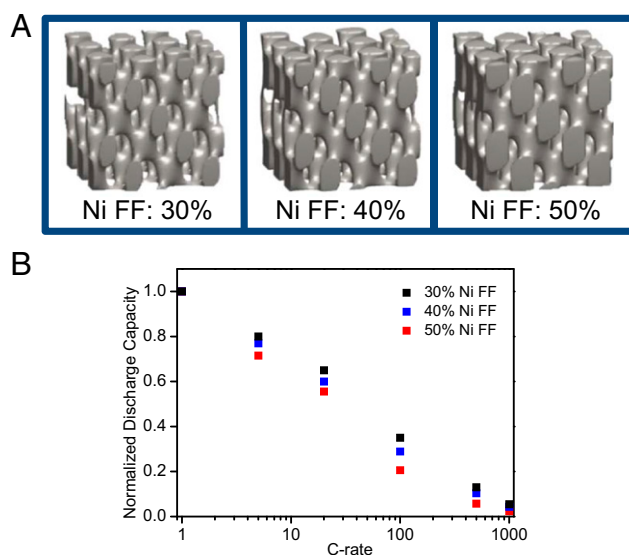

Fig. 5. Influence of electrode porosity on the power performance of 3D microbatteries. (*A*) Schematics of 3D nickel current collectors with various filling fractions (FFs). (*B*) Normalized discharge capacity of microbatteries with various nickel FFs at C rates ranging from 1 to 1,000.

ENGINEERING

densities as well as excellent potential for practical applications. By carefully matching the electrode capacities and precycling the anode to form a necessary SEI layer, the cycle life of the full cell is much improved compared with previous works. The experiments and modeling suggest that the energy and power of the microbattery are strongly related to the structural parameters of the electrodes such as size, shape, surface area, porosity, and tortuosity. A significant strength of the method presented here is that these parameters can be easily controlled during lithography steps, which offers unique flexibility for designing next-generation on-chip energy storage devices.

Materials and Methods

Fabrication of Interdigitated 3D Porous Nickel Scaffolds. The preparation of 3D holographic templates begins with spin-coating (1,500 rpm, 30 s) SU-8 2015 (Micro-Chem) onto ITO substrates (Delta Technologies, sheet resistance: ~100 Ω). To increase the photosensitivity of SU-8 at 532 nm, the photoresist is doped with 0.5 wt % solid content of photoinitiator, cyclopentadienyl(fluorene) iron(II) hexafluorophosphate (Aldrich). The SU-8 film is then exposed to four interfering laser beams arranged in an umbrella geometry for 0.5 s (27). After development, the 3D lattice is hard-baked at 95 °C for 15 min and subsequently infiltrated with the positive photoresist AZ9260 (Microchemicals) by spin-coating (3,000 rpm, 50 s). The infilled AZ9260 resist is photopatterned using a standard photolithography procedure and then hard-baked at 125 °C for 2 min. Next, nickel electrodeposition is performed potentiostatically at −2 V in a commercial sulfamate nickel plating solution (Transene, SN-10), which is followed by removing the polymer template by O$_2$ RIE (20 sccm) with 500-mtorr pressure and 200-W power for 1 h and sequentially revealing the interdigitated 3D nickel current collectors.

Deposition and Processing of Active Materials. Before electrodeposition, the scaffold is briefly washed in a dilute HCl solution to remove the nickel oxide introduced during RIE. Ni–Sn is pulse-plated (0.2 s at –0.22 V, 10 s off) onto one electrode as anode in an electrolyte composed of 0.06 M NiCl$_2$, 0.2 M SnCl$_2$, 1 M K$_4$P$_2$O$_7$, 0.04 M potassium sodium tartrate, and 0.04 M glycine. MnO$_2$ is then electroplated (0.2 s at 1.8 V, 10 s off) onto the other electrode as cathode using a plating solution that contains 0.1 M Na$_2$SO$_4$, 0.1 M CH$_3$COONa, and 0.1 M MnSO$_4$. To lithiate the electrolytic MnO$_2$, a small amount of LiNO$_3$/LiOH molten salt (1:1 molar ratio) is selectively placed onto the microbattery and heated at 300 °C for 30 min. Once the sample is cooled to room temperature, it is rinsed with deionized water and dried at 150 °C in Ar for 2 h. The anode is then precycled independently six times versus lithium metal at 1 C in a 1 M LiClO$_4$ electrolyte (1:1 mass ratio ethylene carbonate:dimethyl carbonate). The full cell is finally capped with PDMS and glass and sealed with UV-curable resin (Addison Clear Wave, AC A1705-TX).

1. Arthur TS, et al. (2011) Three-dimensional electrodes and battery architectures. *MRS Bull* 36(7):523–531.
2. Chen JM, Johansson KH, Olariu S, Paschalidis IC, Stojmenovic I (2011) Special issue on wireless sensor and actuator networks. *IEEE Trans Automat Contr* 56(10):2244–2246.
3. Lemmerhirt DF, Wise KD (2006) Chip-scale integration of data-gathering microsystems. *Proc IEEE* 94(6):1138–1159.
4. Sodano HA, Inman DJ, Park G (2005) Comparison of piezoelectric energy harvesting devices for recharging batteries. *J Intell Mater Syst Struct* 16(10):799–807.
5. Bryzek J, et al. (2006) Marvelous MEMS - Advanced IC sensors and microstructures for high-volume applications. *IEEE Circuits Device* 22(2):8–28.
6. Haque RM, Wise KD (2011) A 3D implantable microsystem for intraocular pressure monitoring using a glass-in-silicon reflow process. *Micro Electro Mechanical Systems (MEMS), 2011 IEEE 24th International Conference* (IEEE, New York), pp 995–998.
7. Mc Caffrey C, Chevalerias O, O'Mathuna C, Twomey K (2008) Swallowable-capsule technology. *IEEE Pervasive Comput* 7(1):23–29.
8. Hodgins D, et al. (2008) Healthy aims: Developing new medical implants and diagnostic equipment. *IEEE Pervasive Comput* 7(1):14–21.
9. Patil A, et al. (2008) Issue and challenges facing rechargeable thin film lithium batteries. *Mater Res Bull* 43(8–9):1913–1942.
10. Nathan M, et al. (2005) Three-dimensional thin-film Li-ion microbatteries for autonomous MEMS. *J Microelectromech Syst* 14(5):879–885.
11. Chamran F, Yeh Y, Min HS, Dunn B, Kim CJ (2007) Fabrication of high-aspect-ratio electrode arrays for three-dimensional microbatteries. *J Microelectromech Syst* 16(4):844–852.
12. Wang CL, et al. (2004) C-MEMS for the manufacture of 3D microbatteries. *Electrochem Solid St* 7(11):A435–A438.
13. Baggetto L, Knoops HCM, Niessen RAH, Kessels WMM, Notten PHL (2010) 3D negative electrode stacks for integrated all-solid-state lithium-ion microbatteries. *J Mater Chem* 20(18):3703–3708.
14. Min HS, et al. (2008) Fabrication and properties of a carbon/polypyrrole three-dimensional microbattery. *J Power Sources* 178(2):795–800.
15. Wang W, et al. (2012) Three-dimensional Ni/TiO2 nanowire network for high areal capacity lithium ion microbattery applications. *Nano Lett* 12(2):655–660.
16. Tan S, Perre E, Gustafsson T, Brandell D (2012) A solid state 3-D microbattery based on Cu2Sb nanopillar anodes. *Solid State Ion* 225:510–512.
17. Chen Y, et al. (2013) Hollow carbon-nanotube/carbon-nanofiber hybrid anodes for Li-ion batteries. *J Am Chem Soc* 135(44):16280–16283.
18. Bruce PG, Scrosati B, Tarascon JM (2008) Nanomaterials for rechargeable lithium batteries. *Angew Chem Int Ed Engl* 47(16):2930–2946.
19. Zhang H, Yu X, Braun PV (2011) Three-dimensional bicontinuous ultrafast-charge and -discharge bulk battery electrodes. *Nat Nanotechnol* 6(5):277–281.
20. Zhang H, Braun PV (2012) Three-dimensional metal scaffold supported bicontinuous silicon battery anodes. *Nano Lett* 12(6):2778–2783.
21. Liu J, et al. (2014) Hydrothermal fabrication of three-dimensional secondary battery anodes. *Adv Mater* 26(41):7096–7101.
22. Pikul JH, Gang Zhang H, Cho J, Braun PV, King WP (2013) High-power lithium ion microbatteries from interdigitated three-dimensional bicontinuous nanoporous electrodes. *Nat Commun* 4:1732.
23. Gratson GM, Xu M, Lewis JA (2004) Microperiodic structures: Direct writing of three-dimensional webs. *Nature* 428(6981):386.
24. Deubel M, et al. (2004) Direct laser writing of three-dimensional photonic-crystal templates for telecommunications. *Nat Mater* 3(7):444–447.
25. Park SG, Miyake M, Yang SM, Braun PV (2011) Cu(2)O inverse woodpile photonic crystals by prism holographic lithography and electrodeposition. *Adv Mater* 23(24):2749–2752.
26. Jeon S, et al. (2004) Fabricating complex three-dimensional nanostructures with high-resolution conformable phase masks. *Proc Natl Acad Sci USA* 101(34):12428–12433.
27. Chen YC, Geddes JB, Lee JT, Braun PV, Wiltzius P (2007) Holographically fabricated photonic crystals with large reflectance. *Appl Phys Lett* 91(24):241103.
28. Miyake M, Chen YC, Braun PV, Wiltzius P (2009) Fabrication of three-dimensional photonic crystals using multibeam interference lithography and electrodeposition. *Adv Mater* 21(29):3012.
29. Zhang HG, Shi T, Braun PV (2015) 3D scaffolded nickel-tin Li-ion anodes with enhanced cyclability. arXiv:1504.07047.
30. Xu K (2004) Nonaqueous liquid electrolytes for lithium-based rechargeable batteries. *Chem Rev* 104(10):4303–4417.
31. Marquardt K, et al. (2010) Development of near hermetic silicon/glass cavities for packaging of integrated lithium micro batteries. *Microsyst Technol* 16(7):1119–1129.
32. Lai W, et al. (2010) Ultrahigh-energy-density microbatteries enabled by new electrode architecture and micropackaging design. *Adv Mater* 22(20):E139–E144.
33. Winter M, Besenhard JO (1999) Electrochemical lithiation of tin and tin-based intermetallics and composites. *Electrochim Acta* 45(1-2):31–50.
34. Kamali AR, Fray DJ (2011) Tin-based materials as advanced anode materials for lithium ion batteries: A review. *Rev Adv Mater Sci* 27(1):14–24.
35. Zhang WJ (2011) A review of the electrochemical performance of alloy anodes for lithium-ion batteries. *J Power Sources* 196(1):13–24.
36. Sun K, et al. (2013) 3D printing of interdigitated Li-ion microbattery architectures. *Adv Mater* 25(33):4539–4543.
37. Nemati Hayati A, Ahmadi MM, Mohammadi S (2012) How particle shape affects the flow through granular materials. *Phys Rev E Stat Nonlin Soft Matter Phys* 85(3 Pt 2):036310.
38. Park J, et al. (2012) Three-dimensional nanonetworks for giant stretchability in dielectrics and conductors. *Nat Commun* 3:916.
39. Liu J, et al. (2015) Mechanically and chemically robust sandwich-structured C@Si@C nanotube array Li-ion battery anodes. *ACS Nano* 9(2):1985–1994.
40. Denning RG, et al. (2011) The control of shrinkage and thermal instability in SU-8 photoresists for holographic lithography. *Adv Funct Mater* 21(9):1593–1601.
41. Peterman MC, Huie P, Bloom DM, Fishman HA (2003) Building thick photoresist structures from the bottom up. *J Micromech Microeng* 13(3):380–382.
42. Voigt A, Heinrich M, Gruetzner G (2004) Characterization of new ultra thick chemically amplified positive tone photoresists suitable for electroplating application. *Proc SPIE* 5376:915–923.